Upscaled laser synthesis of copper nanoparticles in acetone to correlate the surface modification of Nd-Fe-B feedstock properties with part properties after full melting and rapid solidification

Philipp Gabriel[1], Jianing Liu[2], Franziska Staab[3], René Streubel[1], Matthias Miertz[1], Karsten Durst[3], Oliver Gutfleisch[2], Stephan Barcikowski[1]*, Anna Ziefuss[1]

[1] Technical Chemistry I and Center for Nanointegration Duisburg-Essen (CENIDE), University of Duisburg-Essen, 45141 Essen, Germany

[2] Functional Materials, Institute of Material Science, Technical University of Darmstadt, 64287 Darmstadt, Germany

[3] Physical Metallurgy, Institute of Material Science, Technical University of Darmstadt, 64287 Darmstadt, Germany

* corresponding author: stephan.barcikowski@uni-due.de

Keywords:

Laser ablation in liquid
Nanoadditivation
Microstructure
Hard magnets
Additive Manufacturing
Laser Powder Bed Fusion

Abstract

The possibilities of nanoadditivation to achieve finer, more equiaxed grains unlock huge potential for the application field of functional materials, e.g. Nd-Fe-B magnets, where the control of the microstructure and the composition is of significant importance. The surface modification of hard magnetic microparticles by non-magnetic nanoparticles (NPs) opens a novel field of research. Here, especially Cu NPs with low amounts of oxides are of high relevance as colloidal nano-additive material. To increase the productivity of surfactant-free, laser-generated Cu NPs, we performed a process parameter study via laser ablation in acetone aiming for the highest possible productivity, increasing the throughput of NP additivation on the surface of functional feedstock micro powders. By optimizing the process parameters of laser power, laser fluence, repetition rate, volume flow, and spot size, a productivity of 0.19 µg/J of Cu NPs in acetone was achieved. Then we investigated how a fine microstructure of the magnet powder MQP-S can be retained to some extent along the process chain, throughout the melting and resolidification process during suction casting. A loading series of Cu NP nanoadditivation on magnet micro powders of 0.1, 0.5, 1.0, and 2.5 wt.% was analyzed regarding magnetic properties and microstructure of the as-built part. Using full melting conditions of MQP-S by producing samples via suction casting modified with different amounts of Cu NP additions leads to finer grains, but increasing α-Fe content. Overall, the results enable higher production rates of Cu NPs in acetone and provide insights into the influence of NP-supporting characteristics on the properties of permanent magnet micro powders after full melting and resolidification.

Introduction

Metal nanoparticles (NPs) have unique properties, which makes them useful for many applications, such as catalysis [1, 2], biotechnology [3, 4], and modifying feedstock materials within e.g., powder bed fusion using a laser beam (PBF-LB) [5, 6], which enables small series production of fully dense metallic parts with high geometrical freedom, good dimensional accuracy, and reasonable surface finish [7]. Here, however, currently, available metal powder feedstocks have been developed over the last decades for conventional Powder Metallurgy production routes, such as hot compaction, pressing, and sintering or Metal Injection Molding. These feedstocks are not designed for PBF-LB, which differs significantly in their complex melting and rapid solidification behavior. This material-process mismatch leads to typical defects in the microstructure, like lack of fusion porosity, microstructural inhomogeneities, and formation of columnar grains when processing them via PBF-LB.[8, 9] In this context, researchers have shown that nanoadditivation can overcome some of these issues and lead to finer, more equiaxed grains with improved mechanical properties, as the NPs have an impact on the microstructure formation and composition during melting and solidification.[10, 11]

Nanoadditivation can lead to finer, more equiaxed grains which is especially beneficial for the application field of functional materials, e.g., Nd-Fe-B magnets, where the control of the microstructure and chemical composition is of significant importance.[12, 13] Here, especially Cu NPs are of high relevance due to I) their low melting point and melt solubility leading to a good intermixing with rare earth elements (Nd, Pr) [14, 15], and II) their impact on the wettability of grains [16], both leading to an improved microstructure and functional properties.[14, 15] The surface modification of hard magnetic microparticles (MPs) by non-magnetic NPs opens a novel field of research. While the addition of Cu has been well investigated for Nd-Fe-B samples where the Cu has been added via alloying [17], and different types of diffusion processes [15, 18] it is less investigated via the addition of NPs on the hard magnetic particle surfaces.

Although a variety of methods, like wet chemical synthesis, are currently available for the preparation of metal NPs, one common drawback is that the produced NPs carry organic stabilizers on their surface.[19] While surface-bound organic ligands stabilize Cu NPs in a good manner [20] they critically affect their deposition on e.g. microparticle feedstocks and affect for example the powder flowability [6], which is fundamentally required for the application field of PBF-LB [11]. Moreover, organic stabilizers may degrade during melting (bearing the risk of creating gases that locally cause “popcorn” effects) and cause unwanted balling effects, as has been shown in a screening study on dispersant agent effects on laser direct-writing of Ag particle inks [21]. In contrast to wet chemical methods, the production route via laser ablation in liquids (LAL) does not require chemical precursors and allows to produce NPs without organic ligands or steric stabilizers.[22] Here, an ultra-short pulsed laser is applied to ablate a solid metal target in liquids, using laser intensities above a certain threshold which promotes material removal from the target surface.[22] The removed material is collected in the surrounding liquid forming a colloidal dispersion of NPs. Note that LAL is more economical than wet chemical synthesis, but only if gram-scale production can be achieved and post-treatment steps like centrifugation-cleaning are omitted.[23] The productivity of this synthesis route is dependent on a variety of factors like process parameters (ablation time, laser parameters) [22, 24], material density [25], and colloidal environment [26]. While dense materials like Pt (21.1 g/cm³) and Au (19.3 g/cm³) yield laser energy-specific productivity rates in the range of 5.4 [27] – 13.1 [28] µg/J and

5.2[27] – 5.8[28] µg/J, respectively, the production of lighter materials like Ag (10.5 g/cm³) or Cu (9.0 g/cm³) shows an immensely decreased productivity of 2.5 µg/J [27] and 1.8 µg/J [27]. Note that these energy-specific productivity values (mass per ablation time and laser power) are used for better comparison between laser systems with different output power. The absolute LAL productivity values are in the upper g/h scale, e.g. 8.3 g/h for Pt NPs. [28] Taking the final aim of surface-additivated MPs into account, 1 g/h NP productivity would allow a 0.1 wt.% nano-additivated micro powder throughput of 1 kg/h.

These productivities are achieved in aqueous environments, which leads to the rapid formation of oxides on the surface of the NPs.[29] But the reduction of Cu-oxides is required for the application in Nd-Fe-B, as oxides decrease the functional properties because the hcp Nd-rich phase is replaced by fcc Nd oxide, which does not form the required low-temperature eutectic with Cu.[30, 31] However, the number of oxides can be reduced by applying organic solvents to suppress this reaction leading to elemental Cu NPs [32], but such solvents are known to reduce the ablation rates because of cavitation bubble shielding or viscosity effects [33].

To overcome this drawback, in this study, we performed a process parameter study of laser-generated Cu NPs via LAL in acetone, aiming for the highest possible energy-specific productivity and enabling the high-throughput modification of functional feedstock powders. Therefore, we performed the ablation in a flow-through chamber under variation of the laser fluence (by changing the laser pulse energy and spot size), repetition rate, and volume flow of the colloid. The surface modification we conducted here is a fundamental study of how a fine nanocomposite structure, specifically our feedstock MP material MQP-S, can be preserved to some extent throughout a melting and rapid resolidification process. Therefore, we analyzed the influence of a loading series of Cu NPs (nanoadditivation of 0.1, 0.5, 1.0, and 2.5 wt.%) on the feedstock magnet MPs and investigated the influence on the microstructure and magnetic properties of the as-built part. Suction casting (SC) has been selected to produce samples, as it was shown by Schäfer et al. [34] that it leads to phases and grain sizes, which are comparable to additively produced samples, making it a powerful technique to pre-screen materials for the PBF-LB process.

Materials and Methods

In this study, the Cu NPs were prepared by laser ablation in liquids (LAL), where the laser was used to ablate the surface of a Cu-target (20mm (width) x 80mm (length) x 2mm (thickness)) with 99.99% purity, immersed in commercial acetone (Acetone ≥ 99.8%, VWR Int.) containing no further stabilizers. For LAL a ns-pulsed Nd:YAG laser (Innoslab, IS400-1-L, Egdewave GmbH) with 220 W maximum output power was used. The fundamental wavelength was 1064 nm, with a laser pulse duration of 8 ns and a maximum pulse repetition rate of 10 kHz. A galvanometer scanner (intelliSCAN-20, Scanlab AG) with a scanning speed of 3 m/s and a telecentric F-theta lens focusing optics with f = 100 mm and a total transmission at 1030 – 1080 nm of >96% was employed, schematically shown in Figure 1.

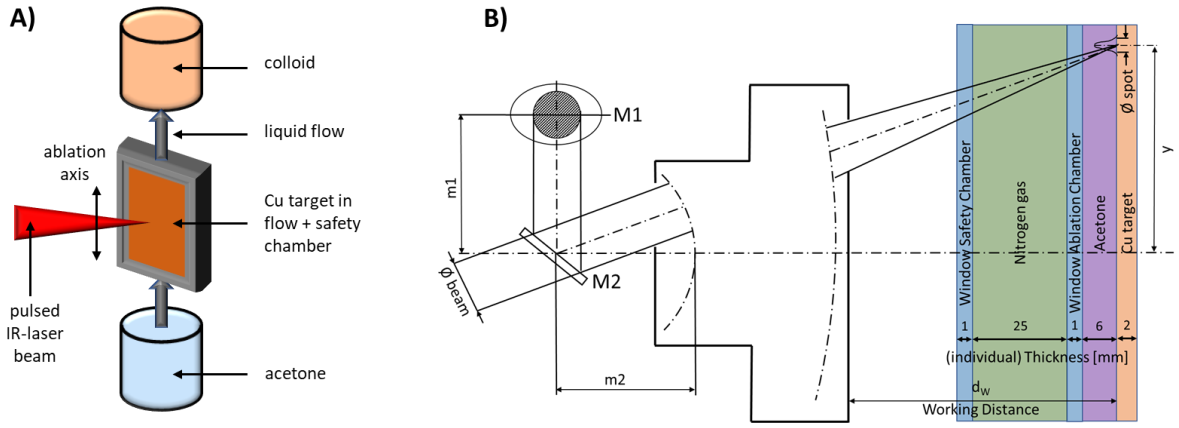

Figure 1 A) Illustration of the applied ablation setup B) using an Nd:YAG laser directed into a galvanometer scanner with a telecentric F-theta lens focusing the laser beam through the window of a safety chamber filled with Nitrogen gas and an ablation chamber window entering the liquid layer of the flow-trough chamber filled with acetone, focused onto the Cu target, with M1 and M2 being the first and second mirrors and m1 and m2 being the recommended mirror distances of 13 – 17 mm and 28 mm, respectively. Note, that though the given values of distances are correct, the size scales are not necessarily reflecting real sizes.

We measured the lateral size of the incident laser spot at the immersed target via a camera setup to be 2.41 mm in horizontal direction (X-axis) and 2.76 mm in vertical direction (Y-axis) and calculated the laser spot size S_S [mm²] via $S_s = \pi \cdot X_i \cdot Y_i$, with $X_i = \frac{(d_{w,max} - d_{w,set})}{\tan \beta_x}$ and $Y_i = \frac{(d_{w,max} - d_{w,set})}{\tan \beta_y}$ with $d_{w,max}$ = 137 mm being the maximum working distance for the used ablation setup, $d_{W,set}$ = 112 to 124 mm in steps of 2 mm being the investigated working distances and $\beta_x = \tan^{-1} \frac{d_{w,max}}{2.41}$ and $\beta_y = \tan^{-1} \frac{d_{w,max}}{2.76}$. To ensure a stab e ablation process during the process parameter studies the laser has been ablating for 5 minutes discarding this run-in-time colloid after which the ablation process ran until the product collection vessel has been filled with 100 mL colloid. Then the resulting colloid has been analyzed via UV-Vis extinction spectroscopy (Evolution 201/220, Thermo Fisher Scientific Inc.) with a spectral bandwidth of 2 nm and intensity-calibrated linearity up to ~1 absorbance, using the pure acetone or water, respectively, as the baseline. The hydrodynamic diameter of the synthesized NPs (see Figure S 4 in section 2 of the SI) was measured by analytical disc centrifugation (ADC, CPS instruments Inc.) at a centrifugation speed of 24,000 rpm with a lower detection limit of 3 nm. Photographs of the LAL setup can be found in the supporting information (SI, Figure S 1).

A gas-atomized Nd-Fe-B-based spherical powder manufactured by Magnequench (part of Neo Performance Materials) was used. The powder is commercially known as MQP-S-11-9-20001 (hereinafter referred to as MQP-S) with a nominal chemical composition of $Nd_{7.5}Pr_{0.7}Zr_{2.6}Ti_{2.5}Co_{2.5}Fe_{75}B_{8.8}$ at.% [35] and particle diameter distribution in µm of D_{10} = 19.01, D_{50} = 38.93 and D_{90} = 64.94. Characterization of the powder size distribution (see Figure S 4 in section 2 of the SI) and morphology was performed by scanning electron microscopy (SEM, Philips ESEM-XL30 FEG, 20kV) equipped with an energy dispersive X-ray detector (EDX) used for the evaluation of the material composition.

The nanoadditivation was performed by colloidal deposition of the Cu NPs onto the surface of the MQP-S MPs via evaporation of the acetone. First, the 10 mg/l colloid was pre-concentrated to approximately 20 ml using a rotary evaporator (Hei-VAP-Core from Heidolph) with the settings of 40°C, 375 hPa, and 100 rotations per minute. Then 5 g of the MQP-S powder was added to the concentrated colloid. The mixture was stirred overnight and the resulting slurry was dried for 8 h using a vacuum drying cabinet (VD-23, Binder GmbH) at 70°C. By varying the NP: MP ratio surface-additivated magnet powder feedstocks with different loadings of Cu NPs (0.1, 0.5, 1.0, and 2.5 wt.%) were prepared.

The prepared powder was processed by suction casting (SC). SC requires 3-4 orders of magnitude lower feedstock material mass compared to PBF-LB, allowing resource-efficient pre-screening of melting-resolidification behavior. It is known that SC has far higher cooling rates (up to 10^2 K/s, depending on the apparatus parameters like critical section thickness as well as material properties) [36] than conventional casting. But the heat gradients and cooling rates of 10^6-10^7 K/s [37], as well as the solidification rates (e.g. 0.5 m/s for Ti-6Al-4V [39]) of PBF-LB, are different from SC. Still, both processes cause full melting and rapid solidification of the nanoadditivated MP feedstock. In that context, it is worth mentioning that SC is able to “emulate” the achieved phases and grain sizes of the PBF-LB process to a certain extent.[34]

To prepare the powder for the suction casting system (MAM-1, Buehler), the Cu NP/MQP-S powder was pre-pressed into a crucible. The material was then molten by an electric arc struck under a protective Ar atmosphere and sucked into a water-cooled mold ending up with bulk rectangular plates with a thickness of 0.5 mm. A two-step annealing heat treatment, which is a standard process for Nd-Fe-B magnets, is applied to increase the coercivity of the manufactured parts. First, the samples are annealed at 1000°C for 5 h with subsequent cooling in air. Then, a second annealing at 500°C for 3 h is applied and the material is cooled down in the furnace. To determine the magnetic performance of the developed magnets, isothermal magnetization measurements were performed using a physical property measurement system (PPMS-VSM, Quantum Design PPMS-14) at room temperature under an applied magnetic field of up to 3 T.

The chemical and structural characterization of the obtained powder feedstocks and the bulk SC samples was carried out via scanning electron microscopy (SEM, TESCAN Mira3) by backscattered electron (BSE) imaging and energy-dispersive X-ray spectroscopy (EDX) point scans using 20 kV acceleration voltage. The cross-sections of the bulk SC samples have been investigated in the edge and core areas. Each phase of the microstructure was analyzed at two different spots. Chemical characterization on powder feedstock samples of nanoadditivated

MQP-S has also been performed via wavelength-dispersive X-ray fluorescence spectroscopy (WD-XRF) to support the results received by the surface-sensitive EDX with volume-sensitive WD-XRF.

Results and Discussion

A negative control ablation was performed using parameters for LAL of Cu NPs in deionized water following recent literature [22, 27, 32, 38] using the ablation setup shown in Figure 1, with a spot size S_S of 0.188 mm^2, repetition rate f of 10 kHz, and laser power P_L of 206 W. However, as expected, ablation in water results in strong oxidation of the Cu NPs (Figure 2, yellow curve), which we aim to avoid for the targeted application of functional materials. To overcome this issue, we performed the ablation in acetone, which has been selected as it provides good production rates (~0.06 g/h at a fluence ϕ of ~1 J/cm²) for the ketone types, as shown by Kawasaki [39]. In their study, Kazakevich et al. [29] utilized laser ablation on a bulk Cu target in acetone and proposed the development of significantly thick glassy carbon clouds, which were found to provide long-term stability against oxidation for even relatively small Cu NPs of approximately 10 nm. They particularly emphasized the role of solvent decomposition products, which are produced primarily at the NP surface heated in the laser beam, and thus provide an effective protective shell.[29] Similar findings have been reported by Marzun et al. [32], who suggested that the formation of structures with a graphite layer on the Cu NPs' surfaces is probably due to the pyrolysis of the acetone. Recently, Fromme et al. [40] performed LAL with a systematic series of organic solvents and deduced selection rules for solvents that influence the formation of carbon shells.

In our work, changing the liquid from water to acetone and keeping the same setup and parameters for LAL, leads to the absorbance spectrum shown by the blue curve in Figure 2. While elemental Cu NPs show surface plasmon resonance (SPR) around 585 nm, Cu-oxides and Cu with a protective shell of carbon or graphite absorb light in the region of 300-500 nm.[32, 39, 41, 42] Note that changing the solvent from water to acetone decreased the overall productivity by a factor of 5.67 from 340 mg/h (0.45 µg/J) to 60 mg/h (0.08 µg/J) although using the same settings for the ablation, we succeeded in optimizing the productivity (Figure 2, orange curve) by varying the volume flow rate $\dot{V}_s$, the laser fluence ϕ, the spot size S_S, the laser power P_L, and the repetition rate f. This has been done in consecutive steps to avoid interdependencies influencing the results. The optimization procedure is described in the following.

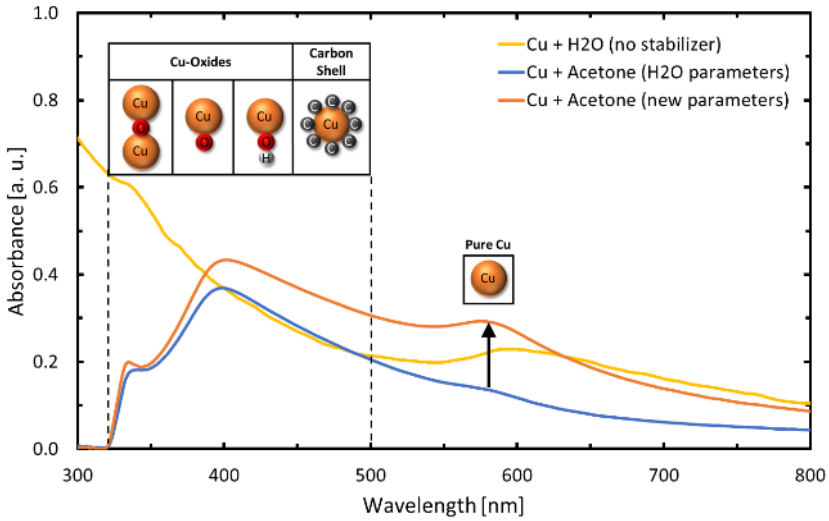

Figure 2 The laser-based synthesis optimization based on UV-Vis extinction spectroscopy. The yellow curve shows the absorbance of the as-produced Cu NPs ablated in water, and the blue and orange curves show the corresponding Cu NPs produced in acetone before (blue) and after (orange) LAL parameter optimization, respectively. Pure Cu NPs absorb light around 585 nm, and the different forms of Cu-oxides and carbon-shelled Cu absorb light in the region of 300-500 nm (regions marked by sketches; size relations and amount of C atoms in carbon shell are not necessarily correct).

Influence of volume flow on the absorbance and productivity of the as-produced colloid

A detailed description of the here applied liquid-flow laser ablation setup with a pump and a vertical flow chamber is shown in Figure S 1 of the SI. Note, that for each of the investigated process parameters we focused on two target values, I) the absorbance at the SPR of Cu NPs (here 585 nm) as proportional to the amount of metallic Cu NPs (the full UV-Vis spectra for all investigated parameters are shown in Figure S 2 of the SI) and II) the mass ablation rate (measured by weighting the target before and after LAL).

At first, the influence of the volume flow rate $\dot{V}_S$ of the acetone on the Cu NP productivity has been investigated in the range from 25 mL/min up to 100 mL/min, with the findings shown in Figure 3A. Note that we kept all other parameters constant at the initially used values (blue curve, Figure 2) for this test (spot size S_S of 0.188 mm², repetition rate f = 10 kHz, laser power P_L = 206 W). We found a clear anti-proportional correlation between the absorbance and $\dot{V}_S$. Thus, with increasing $\dot{V}_S$, the absorbance at the SPR decreases significantly, which can be explained by a continuous dilution of the colloidal solution.[22, 27] However, we found an increase in productivity from 35 to 95 mg/h by varying the $\dot{V}_S$ from 25 to 83 mL/min, which is a result of higher flow rates enabling an improved transport rate of the NPs away from the ablation zone reducing the "surface blocking" effect of consecutive laser pulses by already produced NPs.[22, 27] Higher flow rates of 100 mL/min did not further improve the ablation rate. The absorbance values measured at 585 nm decreased with increasing $\dot{V}_S$ (see blue curve in Figure 3A), but the ablation rate only changed slightly from 94.1 to 95.0 mg/h for the corresponding $\dot{V}_S$ of 66 to 83 mL/min. Consequently, the $\dot{V}_S$ that lead to the highest productivity of metallic (plasmon-resonant at 585 nm) Cu NPs, which we labeled as production window (hereafter labeled as P.W.). The P.W. volume flow rate has been set to 66 mL/min for the following parameter variations, resulting in a productivity of 94.1 mg/h (0.13 µg/J), Figure 3A.

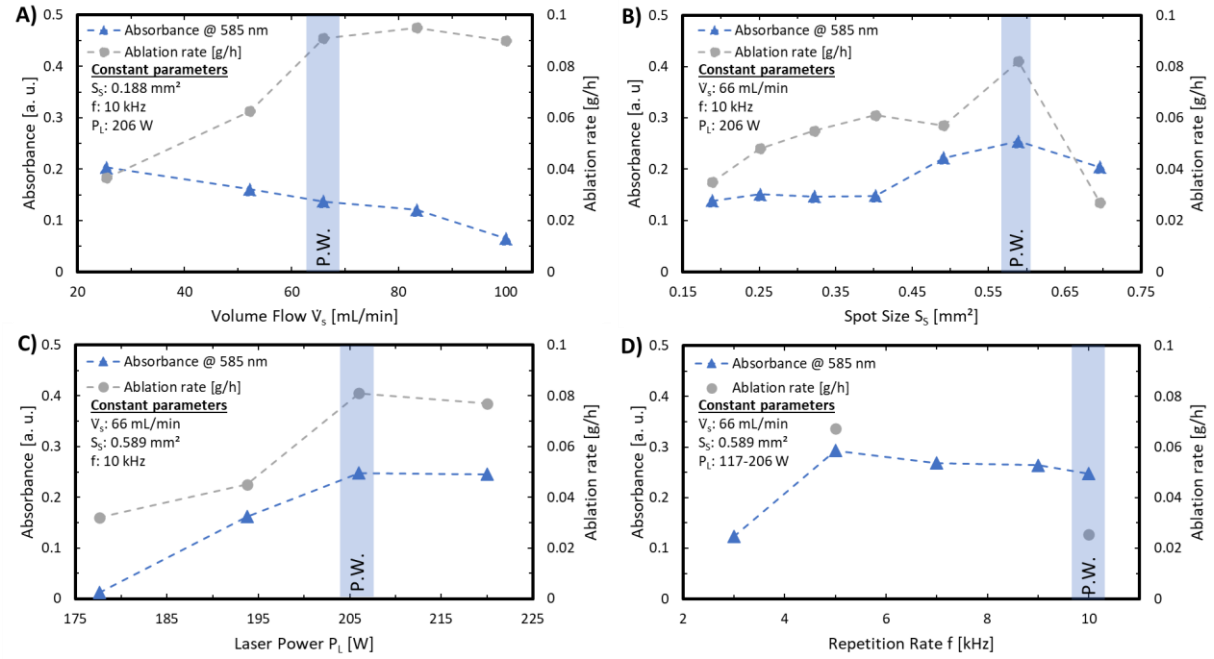

Figure 3 Colloid analysis to determine process parameters for laser ablation of Cu in acetone showing the UV-Vis absorbance values at 585 nm and the corresponding mass ablation rates of 100 mL test colloids, with the constant parameters shown for each parameter test, of A) volume flow $\dot{V}_s$ [mL/min], B) spot size S_S [mm²], C) laser power P_L [W], D) laser pulse repetition rate f [kHz].

Influence of the laser fluence on the absorbance and productivity of the as-produced colloid

The laser fluence ϕ can be varied by changing I) the spot size S_S (see Figure 3B) as it critically influences the laser ablated area and II) the laser power P_L (see Figure 3C). In the following, we will first concentrate on the spot size S_S, which can be influenced in the experimental setup by changing the working distance d_w (distance between the scanner and the bulk target, see Figure 1), and observe its influence on the absorbance and productivity of the as-produced colloid. Here, we fixed the $\dot{V}_s$ to the P.W. evaluated above (66 mL/min) and kept P_L and repetition rate f unchanged (206 W, 10 kHz). The applied ablation setup enabled the change of d_w from 112 to 124 mm, resulting in a change of S_S from 0.696 to 0.188 mm². While the S_S of 0.696 mm² (corresponding to a fluence ϕ of 6.0 J/cm²) leads to only 27 mg/h (0.04 µg/J) ablation rate, the S_S of 0.188 mm² (corresponding to ϕ of 22.3 J/cm²) leads to 35 mg/h (0.05 µg/J) accompanied by a weaker increase in the SPR peak intensity. The ablation at S_S of 0.589 mm² (ϕ of 7.0 J/cm²) shows a significant increase in the absorbance at the SPR, as well as in the ablation rate, which leads to the productivity of Cu NPs of 82 mg/h (0.11 µg/J). The increase in ablation rate is expected to result from the laser energy being used most efficiently for the ablation of the bulk Cu target, with smaller spot sizes ablating a smaller area and removing less material from the target. Too large spot sizes lead to smaller fluence ϕ values because the same energy is projected onto a larger target area (see corresponding fluence values above), and the lower laser fluences ϕ of 6.0 J/cm² lead to a lower ablation rate than ϕ of 7.0 J/cm². The increase in the absorbance spectra at 585 nm can be explained by the findings of Nath et al. [41], who could show that low fluences for the ablation of Cu in water lead to lower pressure at the target surface area, which reduces the material covalency at the copper-water interface, limits full oxidation, and reduces intermolecular interaction. Furthermore, they discussed that high fluences induce higher pressure at the target surface, enabling thermodynamically stable CuO growth. Accordingly, the P.W. has been set at an S_S of 0.589 mm².

Besides, the laser fluence ϕ can be influenced by the laser power P_L, which has been investigated by using the previously determined P.W.s for $\dot{V}_s$ and S_S (66 mL/min, 0.589 mm²) and keeping the repetition rate f constant at 10 kHz. Here, the absorbance at 585 nm increases with increasing P_L, reaching its maximum at 206 W (Figure 3C) with productivity increasing from 32 to 81 mg/h (178 – 206 W; corresponding fluences ϕ of 6.0 – 7.0 J/cm²). Note that we used a P_L of 206 W during the previous investigations of the S_S as well, and the productivity of 81 mg/h (0.11 µg/J) matches the previous results, confirming the previous parameter test results. A further increase of P_L from 206 W to 220 W (ϕ of 7.5 J/cm²) leads to comparable results of absorbance and productivity. This can be explained by the ablation scaling law [27], which defines a saturation of the overall ablation rate for high fluences and proposes that the ablation rate for metals can be optimized with a maximum energy-specific ablation rate (µg/J) at a theoretical optimum fluence defined by $e^2 \cdot \phi_{th}$ with e being the Euler constant and ϕ_{th} being the threshold fluence. The maximum of the specific ablation rate coincides with $e^2 \cdot \phi_{th}$ and agrees well with the model summarized by Neuenschwander et al. [43] for laser ablation in air and confirmed by Streubel et al. for high-speed LAL [27]. According to this model, the ablation process linearly scales with the average laser power, while higher fluences lead to reduced efficiency. Accordingly, the P.W. has been set at P_L of 206 W.

Influence of the repetition rate on the absorbance and productivity of the as-produced colloid

Finally, the laser pulse repetition rate f has been investigated, as the laser power of the applied ablation setup is modified via the current in [A] and depends on the applied repetition rate f, see Figure S 3 in section 2 of the SI. The determined P.W.s for $\dot{V}_s$ and S_S (66 mL/min, 0.589 mm²) have been applied and f was varied from 3 to 10 kHz with 10 kHz being the upper limit for the used laser device (below 3 kHz no ablation could be measured), shown in Figure 3D. Accordingly, the laser power is limited for a repetition rate f of 3 kHz to 117 W, for 5 kHz to 195 W, and for 10 kHz the maximum of 220 W is reachable. As the laser power P_L of 206 W in combination with f of 10 kHz has been shown to lead to better results than the 220 W option (see Figure 2C) and is accordingly here used as an upper limit. Note that for the repetition rate, the ablation rate has only been investigated at 5 and 10 kHz, and consequently, we refrained from inserting a guide to the eye line. Here, the absorbance spectra at 585 nm show a linear dependency on f reaching saturation above 5 kHz. Wagener et al. [44], received similar results for the ablation of Zn in THF and showed that below 5 kHz, the ablation per pulse is constant. Consequently, the productivity is linear to the repetition rate f. At higher repetition rates (>5 kHz), ablation per pulse decays monoexponentially, leading to a final productivity saturation.[44] They explained this by the temporal bypassing of cavitation bubbles for higher repetition rates. Additionally, this observation can be explained by studies of Nolte et al. [45] and Thorstensen et al. [46], who found that as much as a third (for ps pulse length) of the heat generated during the ablation process remains in the metal target leading to a decrease of ablation rate by roughly 40% when the temperature of the target rises by 300°C. The target-temperature dependence of the ablation threshold was attributed to the temperature-dependent linear absorption coefficient, which is the main contributor to increased electron density.[45] For ns pulses, as used here, Vogel et al. [47] have investigated the energy dissipation of shock waves generated by laser pulses. They showed, for ns pulses, that up to 51% (10 mJ, 6 ns) of the induced laser energy was transferred into a shock wave and caused high local temperatures within a few hundred micrometers around the ablation spot.[47] As the laser power of the applied ablation setup depends

on the applied repetition rate and the optimal P_L can only be achieved when using the highest repetition rate, the application of 10 kHz has been set as P.W.

In summary, combining all parameter optimizations we were able to increase the overall productivity of colloidal, plasmon-resonant Cu NPs in acetone from 60 mg/h (0.08 µg/J) to 140 mg/h (0.19 µg/J), which is an increase of 220% and a good base for producing NP-additivated magnet feedstock micro powders in the multiple-gram scale.

Supporting efficiency of different mass loadings of Cu NPs on Nd-Fe-B

After optimizing the laser parameters towards the high productivity of Cu NPs, we produced a sufficient amount for testing their applicability on functional powder feedstock. We added the NPs to the MQP-S MPs by evaporating the acetone (see details in the method part). Note that the MQP-S MPs show a mass-weighed mean diameter of 38 ± 17 µm, which is selected for reaching good performance in further processing (further details can be found in the method section). Figure 4 shows the nanoadditivated MPs with increasing Cu NP mass load at two different magnifications.

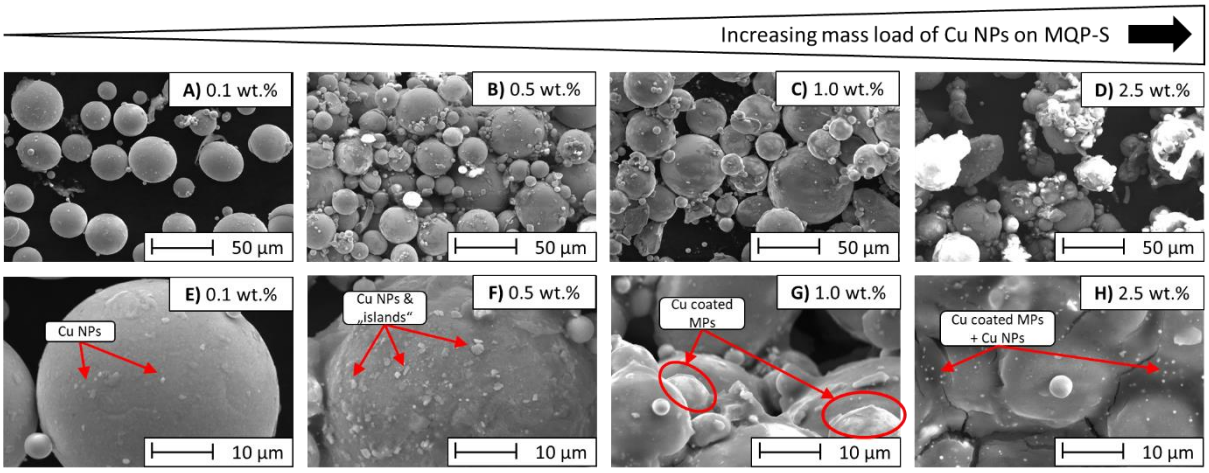

Figure 4 SEM images of the MQP-S microparticles with additions of increasing mass loadings of Cu NPs from left to right (0.1 – 2.5 wt.%), with a magnification of 500x A) - D). Figures E-H) show corresponding high-resolution SEM images with a magnification of 2,500x.

The sample with a mass load of 0.1 wt.% (Figure 4A and E) shows a homogeneous distribution of Cu NPs on the MPs surface. Such homogeneous surface distribution of NPs in MPs is typical for colloidal deposition in the sub-monolayer loading regime [48]. For the mass loadings ≥ 0.5 wt.%, we found increased levels of inhomogeneities in the NPs distribution. With more NPs deposited, they start to agglomerate on the surface of the MPs. As can be seen in the example of 0.5 wt.% Cu NPs addition, these islands become up to a few hundred nanometers in size, with the islands being fairly homogeneously deposited over the MPs surface, except for some MPs, where higher amounts of Cu NPs seem to start forming a full coating, leading to light white areas, shown in Figure 4B and F. Note, that it cannot be fully excluded that these white areas are caused by effects of the SEM analysis, like reflections of the electron beam or charge effects, but for multiple areas investigated and after repetition of the analysis these areas have been found in comparable occurrence. The samples with 1.0 wt.% Cu NPs addition shows less to none of the islands anymore. Still, instead, the MPs seem to have a partial or even full coating, which can be seen by the MPs' surface being smoother when compared to the MPs' surface in the previous

images, shown in Figure 4C and G, respectively. Further increase of Cu NPs to an addition of 2.5 wt.% increases the amount of MPs with complete Cu coatings and also intensifies the coating up to a point where a new layer of scattered Cu NPs on top of the coating can be identified, shown in Figure 4D and H.

The successful Cu NP coating of the MPs has been validated by EDX mappings of the MP surface, shown exemplarily for the sample with 1 wt.% Cu NP loading in Figure 5A-D (EDX mapping of 0.5 wt.% is shown in Figure S 5 of the SI). Additionally applied XRF measurements of the powder feedstocks reveal a correlation of the targeted loading values of Cu NPs on MQP-S MPs with the measured Cu concentration, shown in Figure 5E (see detailed results in Table S 1 of the SI). The measured Cu loading matches the target values up to 1.0 wt.%. At 2.5 wt.% the WD-XRF overestimates the loading, probably as the x-ray penetration depth is affected by the Cu coating thickness.

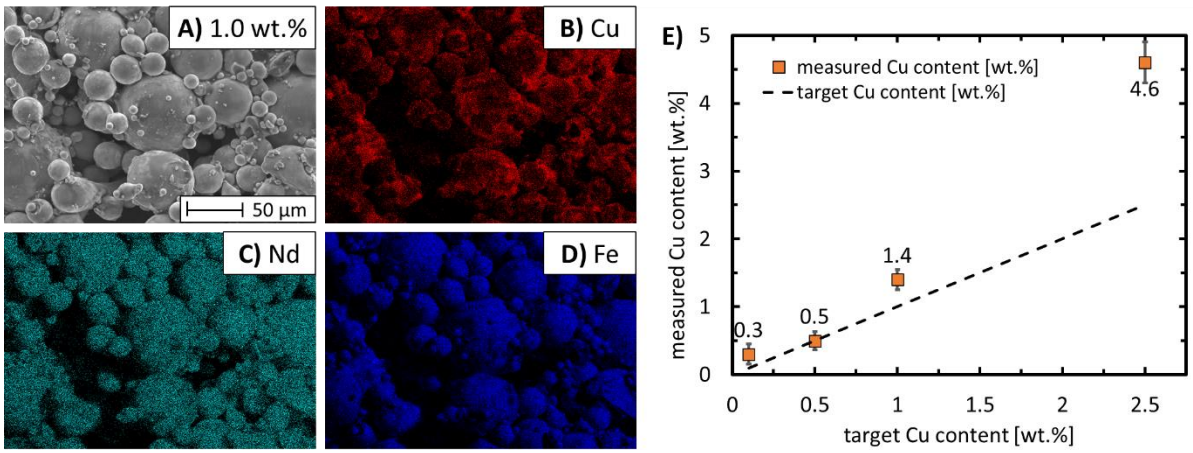

Figure 5 A) – D) EDX mapping of MQP-S MPs decorated with 1.0 wt.% Cu NPs, A) SEM image of the selected area for the analysis of the elements, B) showing an even distribution of Cu on the surface, C) and D) showing the distribution of Nd and Fe of the Nd-Fe-B based powder. E) comparison of the targeted Cu content with the measured Cu content via WD-XRF.

Influence of Cu NPs on the microstructure after suction casting

To investigate how this surface modification enables the preservation of a fine nanocomposite structure (fine-grained microstructure) after melting and resolidification we applied suction casting (SC) to process the prepared powder feedstock. SC simulates the PBF-LB process, as shown by Schäfer et al. [34], by forming similar phases and grain sizes. As mentioned above, the PBF-LB process has far higher cooling rates (process parameter-dependent, 10^3-10^5 K/s)[34] than SC, which at least comes close to this range (10^2 K/s). Additionally, SC is a convenient feedstock pre-screening technique for PBF-LB as only low amounts of material are required. Please refer to the method section for a detailed description of the SC manufacturing process and the applied post-processing.

To get a better understanding of the influence of the Cu NPs on the microstructure and elemental composition, a pure MQP-S sample was analyzed via SEM after SC, shown in Figure 6A. For direct comparison, a sample made of MQP-S with 1 wt.% Cu NPs has been investigated, shown in Figure 6B.

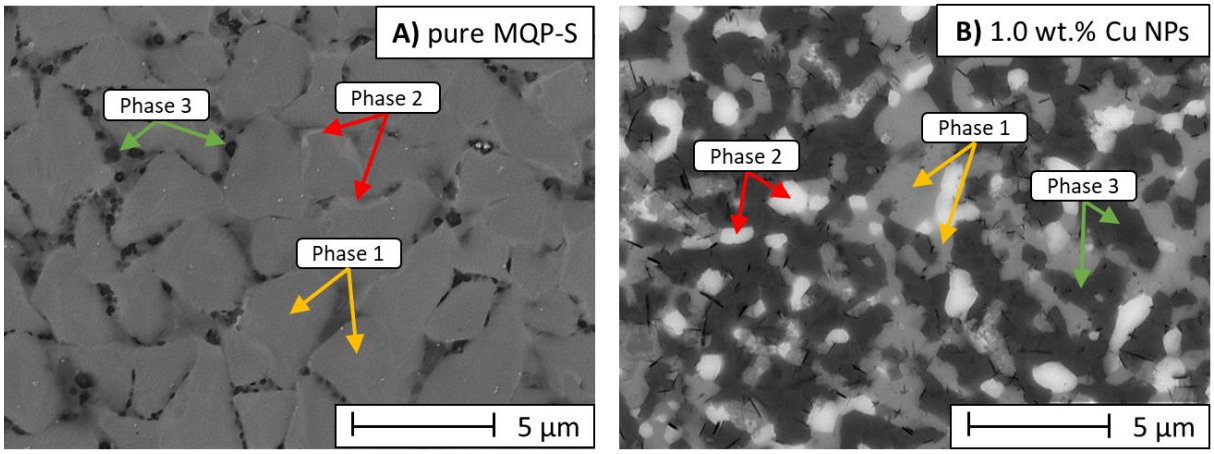

Figure 6 HR-SEM images at a magnification of 10,000x of horizontal (x-y-plane) cross-sections of suction casted samples of A) pure MQP-S without the addition of NPs and B) MQP-S modified with 1 wt.% Cu NP additivation, which both show three main phases as marked.

The SEM analysis shows three different main phases with different distributions, which are marked in Figure 6 for both samples. The sample without the addition of Cu NPs mainly shows the expected $Nd_2Fe_{14}B$ grains (marked as phase 1 in Figure 6A) with comparable sizes of 2-7 µm, which is expected for samples produced via suction casting.[34] The intergranular phase seems to be composed of two different types, of which the first type can be seen as the light grey areas (marked as phase 2 in Figure 6A), which are mainly found at the edges of the $Nd_2Fe_{14}B$ grains but are not Nd-rich as they would be in samples produced via conventional manufacturing technologies [49], which possibly allows more magnetic coupling of the $Nd_2Fe_{14}B$ grains and thereby reducing functionality. Furthermore, there are black circular areas (marked as phase 3 in Figure 6A) within the intergranular phase, which are mainly composed of Fe, Zr, and Ti, and are expected to be enlarged areas of α-Fe, which is soft magnetic, having low coercivity and therefore losing the magnetization rapidly, when applying an external magnetic field in opposite direction.

In Figure 6B the sample with the addition of 1 wt.% Cu NPs shows finer grains of sizes ranging from a few hundred nanometers to 3 µm, possibly a nano-crystallinity, which has been described in other recent studies to be caused by the application of NPs [10, 11] and can be confirmed here for the functional material MQP-S even after full melting and rapid resolidification. Again, the BSE-SEM analysis shows three different phases which are marked in Figure 6B, but with the Nd-rich (phase 2) and the α-Fe (phase 3) phases being more pronounced. Actually, MQP-S is a nanocomposite, meaning a fine mixture of $Nd_2Fe_{14}B$ grains and α-Fe nanograins, after suction casting these phases are still present and have coarsened significantly. Consequently, the impact of Cu NPs on the formation and distribution of microstructural phases needs to be investigated further.

An EDX analysis has been performed o get a better understanding of the influence of the Cu NPs on the elemental composition of an MQP-S sample modified with 1 wt.% Cu NPs. Two EDX measurements of each of the three main phases have been performed and the average results of the corresponding elemental compositions are shown in Table 1.

Table 1 Elemental composition of the three main phases marked in Figure 6B of the MQP-S sample with 1 wt.% Cu NPs

Phase [wt.%]	Nd	Pr	Fe	Cu	Co	Ti	Zr
Phase 1 ferromagnetic $Nd_2Fe_{14}B$ grains	23.60	2.25	68.15	1.00	3.75	0.35	0.90
Phase 2 Nd-rich	57.45	6.75	29.75	0.15	1.35	0.70	3.85
Phase 3 α-Fe.	3.25	0.30	91.7	0.70	3.35	0.65	0.10

Phase 1 are the ferromagnetic $Nd_2Fe_{14}B$ grains, whereas phase 2 corresponds to the Nd-rich intergranular phase, and phase 3 is α-Fe. In conventionally produced Nd-Fe-B magnets the thin amorphous Nd-rich layers do not contain any significant Fe content and therefore are paramagnetic, thereby enabling good exchange decoupling of the $Nd_2Fe_{14}B$ grains. [50, 51] If they contain larger amounts of Fe, they would be ferro- or ferrimagnetic, which would change the impact of pinning effects on the remagnetization process.[52] But in the samples produced via SC, a globular structure can be seen (Figure 6B) and the Nd-rich phase is not surrounding the $Nd_2Fe_{14}B$ grains. Furthermore, it contains almost 30 wt.% Fe and might not be paramagnetic, but ferro- or ferrimagnetic.

The Cu can be found in all phases but is primarily found in phases 1 and 3, while only minor amounts are found in the Nd-rich phase (see Table 1). In other studies, which added Cu to Nd-Fe-B feedstock, it mainly went into the Nd-rich intergranular or the grain boundary phases and could strengthen these thin phases to improve the magnetic decoupling of the ferromagnetic $Nd_2Fe_{14}B$ grains.[15, 18, 31] Please note that the Fe content may be influenced due to the Nd–Fe–Cu ternary eutectic reaction below 600 °C, from which the formation of $Nd_6Fe_{13}Cu$ is possible [53], which here fits the measured composition of phase 1 better than the expected typical 2-14-1 composition.

Furthermore, for this fine microstructure, EDX cannot provide exact values for the composition due to the size of the excitation bulb of the electron beam, which partially overlaps into neighboring phases, giving also a signal of those in addition to the actual phase which should be investigated. Accordingly, it can be assumed that phase 3 is pure α-Fe even though only 91.7 wt.% Fe was detected by EDX. Containing such high amounts of the soft magnetic α-Fe as can be seen in Figure 6B, low coercivity can be expected (see Figure S 6 in section 3 of the SI). This composition has been reported before by other groups [34, 54] using the production technique of SC, who managed to dissolve the α-Fe by applying post-process heat treatments (e.g. 5h at 1000°C + 3h at 500°C [34]), but they used different compositions of Nd-Fe-B alloy based feedstocks. Even though the same heat treatment after SC was applied the α-Fe could not be dissolved in this study, resulting in the following two hypotheses.

I) The origin of the high amount of α-Fe in the samples could be caused by the initially mentioned carbon shell formed around the Cu NPs during ablation in acetone, which is formed by solvent decomposition products. As oxygen and carbon would preferably combine with Nd and Fe, they could lead to a thinner Nd-rich phase along

the grain boundaries and agglomerate into the triple junctions, which leads to more coupled Nd-Fe-B grains and lower coercivity.[55] Sasaki et al. [56] confirmed that for sintered Nd-Fe-B samples, carbon caused Nd-carbide formation and the reduction in the volume fraction of α-Nd at the triple junctions. Furthermore, the carbon is also known to affect the eutectic transformations, which explains the Cu content being detectable in all phases.[57] As the carbon shell is preferably combining with the Fe in the Nd-Fe-B powder and increases precipitation of α-Fe, the LAL synthesis of Cu NPs in organic solvents like acetone may not be ideal for the production of NPs for the application of these types of magnets. On the other hand, it is questionable if the carbon amount (i.e. thickness of the carbon shell, or C/Cu ratio, resulting in the effective C doping level of the magnet MPs) is enough to influence the bulk magnet properties. It has been reported for Ni NPs made by LAL in acetonitrile [58] and modeled by Reichenberger et al. [59] for Ni but also compared to experimental values of LAL of Cu in acetone that the carbon shell thickness around LAL-generated NPs is anti-proportional to the NP´s specific surface area. With the quite small NPs yielded in our study (4 nm peak diameter, see Fig. S3 in the SI), only a single-digit number of carbon layers are expected, resulting in a carbon doping level of the magnets in the low ppm range.

II) Furthermore, there might be possible effects of the inhomogeneous distribution of NPs on the surface of the MPs on the microstructure and phase distribution. As mentioned before via SEM, EDX, and XRF analysis, shown in Figure 4 and Figure 5, the NPs start to agglomerate on the surface of the MPs for loadings of 1 wt.% and above. Hence, it would be worth investigating the magnet´s microstructure and phases at lower doping levels, e.g. 0.1 or 0.,5 wt.%, in the future. Those low-loading samples also showed better coercivity and remanence values (see Fig. S5 in the SI) than the higher-loaded samples.

Conclusion

Nanoparticle additivation of micro powders has been shown to positively affect functional properties and the microstructure after melting and rapid resolidification, for example in additive manufacturing by laser powder bed fusion of steel or aluminium alloys. But far less is known about NP effects during magnet powder melt processing. Here, Cu NPs could be an interesting candidate, as Cu is expected to interact with the constituents of Nd-based permanent magnets. A process parameter study of the LAL process for the synthesis of Cu NPs in acetone has been performed and the combination of the volume flow rate of 66 mL/min, spot size of 0.589 mm², laser fluence of 7.0 J/cm,², the repetition rate of 10 kHz and laser power 206 W was identified to lead to the productivity of 140 mg/h (0.19 µg/J). Additionally, this study focused on preferably producing Cu NPs with fewer Cu-oxides by increasing the amount of elemental Cu received after LAL indicated by their surface plasmon resonance intensity. This maximized NP productivity value enables the production of approximately one kilogram of 0.1 wt.% nano-additivated magnet micro powder per day (7 hours), and would be further scaleable with higher laser power.

Next, we investigated in a fundamental study how a fine nanocomposite structure, of our feedstock magnet powder MQP-S, surface-modified with Cu NPs can be retained to some extent throughout a melting and rapid solidification process. Therefore, we analyzed the impact of the surface modification of MQP-S MPs with a Cu NPs loading series (0.1, 0.5, 1.0, and 2.5 wt.%) and its effect on the microstructure of samples produced via suction casting. To our best knowledge, there is no reference for the influence of NP-supporting characteristics

on the properties of MQP-S after full melting, requiring an in-depth investigation of the sample properties after SC. Here, we found that larger loadings (1 and 2.5 wt.%) of Cu NPs tend to agglomerate on the MPs' surface, leading to an uneven distribution of Cu within the samples produced via SC.

The surface modification of (here initially) hard magnetic particles by non-magnetic NPs is the novelty here, which differs from established grain boundary diffusion processes in the literature. Performing experiments using the full melting conditions of this manufacturing process on MQP-S combined with different additions of Cu NPs leads to finer grains, but also increases the α-Fe content. The 0.1 and 0.5 wt.% Cu NP loaded Nd-magnet microparticles showed better magnetic properties after suction casting compared to the high (inhomogeneously coated or "overloaded") Cu NP additivations.

As the LAL productivity increase of this study enabled the production of sufficient amounts of nanoadditivated Nd-Fe-B alloy-based powder feedstock, the gained knowledge can be transferred to the production method of PBF-LB for further tests and to enable the production of larger and also geometrically more sophisticated geometries out of such powders.

Acknowledgments

This work was financially supported by the Deutsche Forschungsgemeinschaft (DFG, German Research Foundation) within the Collaborative Research Centre / Transregio (CRC/TRR) 270, Project ID No. 405553726, subprojects A08, A10, A11. The authors thank Konstantin Skokov from the University of Darmstadt for fruitful discussions concerning the properties of permanent magnets. Furthermore, we thank Murat Ihsan Kusoglu for performing XRF measurements.

Conflicts of interest

The authors declare no conflicts of interest.

References

[1] Newton, M. A. Dynamic Adsorbate/Reaction Induced Structural Change of Supported Metal Nanoparticles: Heterogeneous Catalysis and Beyond. *Chem. Soc. Rev.*, **2008**, *37* (12), 2644–2657. https://doi.org/10.1039/B707746G.

[2] Somorjai, G. A.; Park, J. Y. Colloid Science of Metal Nanoparticle Catalysts in 2D and 3D Structures. Challenges of Nucleation, Growth, Composition, Particle Shape, Size Control and Their Influence on Activity and Selectivity. *Top. Catal.*, **2008**, *49* (3), 126–135. https://doi.org/10.1007/s11244-008-9077-0.

[3] Biju, V.; Itoh, T.; Anas, A.; Sujith, A.; Ishikawa, M. Semiconductor Quantum Dots and Metal Nanoparticles: Syntheses, Optical Properties, and Biological Applications. *Anal. Bioanal. Chem.*, **2008**, *391* (7), 2469–2495. https://doi.org/10.1007/s00216-008-2185-7.

[4] Stein, F.; Kohsakowski, S.; Martinez-Hincapie, R.; Reichenberger, S.; Rehbock, C.; Colic, V.; Guay, D.; Barcikowski, S. Disproportional Surface Segregation in Ligand-Free Gold–Silver Alloy Solid Solution Nanoparticles, and Its Implication for Catalysis and Biomedicine. *Faraday Discuss.*, **2023**, *242* (0), 301–325. https://doi.org/10.1039/D2FD00092J.

[5] Doñate-Buendía, C.; Frömel, F.; Wilms, M. B.; Streubel, R.; Tenkamp, J.; Hupfeld, T.; Nachev, M.; Gökce, E.; Weisheit, A.; Barcikowski, S.; et al. Oxide Dispersion-Strengthened Alloys Generated by Laser Metal Deposition of Laser-Generated Nanoparticle-Metal Powder Composites. *Mater. Des.*, **2018**, *154*, 360–369. https://doi.org/10.1016/j.matdes.2018.05.044.

[6] Hupfeld, T.; Sommereyns, A.; Riahi, F.; Doñate-Buendía, C.; Gann, S.; Schmidt, M.; Gökce, B.; Barcikowski, S. Analysis of the Nanoparticle Dispersion and Its Effect on the Crystalline Microstructure in Carbon-Additivated PA12 Feedstock Material for Laser Powder Bed Fusion. *Materials*, **2020**, *13* (15), 3312. https://doi.org/10.3390/ma13153312.

[7] Kusoglu, I.; Doñate-Buendía, C.; Barcikowski, S.; Gökce, B. Laser Powder Bed Fusion of Polymers: Quantitative Research Direction Indices. *Mater. Basel Switz.*, **2021**, *14*. https://doi.org/10.3390/ma14051169.
[8] Mostafaei, A.; Zhao, C.; He, Y.; Reza Ghiaasiaan, S.; Shi, B.; Shao, S.; Shamsaei, N.; Wu, Z.; Kouraytem, N.; Sun, T.; et al. Defects and Anomalies in Powder Bed Fusion Metal Additive Manufacturing. *Curr. Opin. Solid State Mater. Sci.*, **2022**, *26* (2), 100974. https://doi.org/10.1016/j.cossms.2021.100974.
[9] Ravalji, J. M.; Raval, S. J. Review of Quality Issues and Mitigation Strategies for Metal Powder Bed Fusion. *Rapid Prototyp. J.*, **2022**, *29* (4), 792–817. https://doi.org/10.1108/RPJ-01-2022-0008.
[10] Martin, J. H.; Yahata, B. D.; Hundley, J. M.; Mayer, J. A.; Schaedler, T. A.; Pollock, T. M. 3D Printing of High-Strength Aluminium Alloys. *Nature*, **2017**, *549* (7672), 365–369. https://doi.org/10.1038/nature23894.
[11] Kusoglu, I. M.; Huber, F.; Doñate-Buendía, C.; Rosa Ziefuss, A.; Gökce, B.; T. Sehrt, J.; Kwade, A.; Schmidt, M.; Barcikowski, S. Nanoparticle Additivation Effects on Laser Powder Bed Fusion of Metals and Polymers—A Theoretical Concept for an Inter-Laboratory Study Design All Along the Process Chain, Including Research Data Management. *Materials*, **2021**, *14* (17), 4892. https://doi.org/10.3390/ma14174892.
[12] Gutfleisch, O.; Willard, M. A.; Brück, E.; Chen, C. H.; Sankar, S. G.; Liu, J. P. Magnetic Materials and Devices for the 21st Century: Stronger, Lighter, and More Energy Efficient. *Adv. Mater.*, **2011**, *23* (7), 821–842. https://doi.org/10.1002/adma.201002180.
[13] Coey, J. M. D. *Magnetism and Magnetic Materials*, Paperback edition.; Cambridge University Press: Cambridge New York Port Melbourne, 2018.
[14] Fuerst, C. D.; Brewer, E. G. Diffusion-alloyed Additives in Die-upset Nd-Fe-B Magnets. *J. Appl. Phys.*, **1991**, *69* (8), 5826–5828. https://doi.org/10.1063/1.347862.
[15] Sepehri-Amin, H.; Liu, L.; Ohkubo, T.; Yano, M.; Shoji, T.; Kato, A.; Schrefl, T.; Hono, K. Microstructure and Temperature Dependent of Coercivity of Hot-Deformed Nd–Fe–B Magnets Diffusion Processed with Pr–Cu Alloy. *Acta Mater.*, **2015**, *99*, 297–306. https://doi.org/10.1016/j.actamat.2015.08.013.
[16] Fidler, J.; Bernardi, J. Transmission Electron Microscope Characterization of Cast and Hot-worked R-Fe-B:Cu(R=Nd,Pr) Permanent Magnets. *J. Appl. Phys.*, **1991**, *70* (10), 6456–6458. https://doi.org/10.1063/1.349929.
[17] Li, W. F.; Ohkubo, T.; Akiya, T.; Kato, H.; Hono, K. The Role of Cu Addition in the Coercivity Enhancement of Sintered Nd-Fe-B Permanent Magnets. *J. Mater. Res.*, **2009**, *24* (2), 413–420. https://doi.org/10.1557/JMR.2009.0041.
[18] Akiya, T.; Liu, J.; Sepehri-Amin, H.; Ohkubo, T.; Hioki, K.; Hattori, A.; Hono, K. Low Temperature Diffusion Process Using Rare Earth-Cu Eutectic Alloys for Hot-Deformed Nd-Fe-B Bulk Magnets. *J. Appl. Phys.*, **2014**, *115* (17), 17A766. https://doi.org/10.1063/1.4869062.
[19] Zhang, J.; Chen, G.; Chaker, M.; Rosei, F.; Ma, D. Gold Nanoparticle Decorated Ceria Nanotubes with Significantly High Catalytic Activity for the Reduction of Nitrophenol and Mechanism Study. *Appl. Catal. B Environ.*, **2013**, *132–133*, 107–115. https://doi.org/10.1016/j.apcatb.2012.11.030.
[20] Kanninen, P.; Johans, C.; Merta, J.; Kontturi, K. Influence of Ligand Structure on the Stability and Oxidation of Copper Nanoparticles. *J. Colloid Interface Sci.*, **2008**, *318* (1), 88–95. https://doi.org/10.1016/j.jcis.2007.09.069.
[21] Letzel, A.; Maurer, E.; Meixner, M.; Poprawe, R.; Stollenwerk, J.; Hessner, S.; Lehmann, K.; Gökce, B.; Barcikowski, S. Effect of Various Dispersing Agents on the Stability of Silver Microparticle Dispersion and the Formulation of Uniform Silver Film by Laser Melting. *J. Laser Appl.*, **2016**, *28* (4), 042004. https://doi.org/10.2351/1.4955011.
[22] Zhang, D.; Gökce, B.; Barcikowski, S. Laser Synthesis and Processing of Colloids: Fundamentals and Applications. *Chem. Rev.*, **2017**, *117* (5), 3990–4103. https://doi.org/10.1021/acs.chemrev.6b00468.
[23] Jendrzej, S.; Gökce, B.; Epple, M.; Barcikowski, S. How Size Determines the Value of Gold: Economic Aspects of Wet Chemical and Laser-Based Metal Colloid Synthesis. *ChemPhysChem*, **2017**, *18* (9), 1012–1019. https://doi.org/10.1002/cphc.201601139.
[24] Waag, F. Laser Synthesis of Metallic and Oxidic Transition Metal, Multi-Element Nanoparticles for Catalytic Applications, DuEPublico: Duisburg-Essen Publications online, University of Duisburg-Essen, Germany, 2019. https://doi.org/10.17185/DUEPUBLICO/71120.
[25] Streubel, R.; Bendt, G.; Gökce, B. Pilot-Scale Synthesis of Metal Nanoparticles by High-Speed Pulsed Laser Ablation in Liquids. *Nanotechnology*, **2016**, *27* (20), 205602. https://doi.org/10.1088/0957-4484/27/20/205602.
[26] Kalus, M.-R.; Lanyumba, R.; Lorenzo-Parodi, N.; Jochmann, M. A.; Kerpen, K.; Hagemann, U.; Schmidt, T. C.; Barcikowski, S.; Gökce, B. Determining the Role of Redox-Active Materials during Laser-Induced Water Decomposition. *Phys. Chem. Chem. Phys.*, **2019**, *21* (34), 18636–18651. https://doi.org/10.1039/C9CP02663K.

[27] Streubel, R.; Barcikowski, S.; Gökce, B. Continuous Multigram Nanoparticle Synthesis by High-Power, High-Repetition-Rate Ultrafast Laser Ablation in Liquids. *Opt. Lett.*, **2016**, *41* (7), 1486–1489. https://doi.org/10.1364/OL.41.001486.
[28] Waag, F.; Streubel, R.; Gökce, B.; Barcikowski, S. Synthesis of Gold, Platinum, and Gold-Platinum Alloy Nanoparticle Colloids with High-Power Megahertz-Repetition-Rate Lasers: The Importance of the Beam Guidance Method. *Appl. Nanosci.*, **2021**, *11* (4), 1303–1312. https://doi.org/10.1007/s13204-021-01693-y.
[29] Kazakevich, P. V.; Voronov, V. V.; Simakin, A. V.; Shafeev, G. A. Production of Copper and Brass Nanoparticles upon Laser Ablation in Liquids. *Quantum Electron.*, **2004**, *34* (10), 951. https://doi.org/10.1070/QE2004v034n10ABEH002756.
[30] Mazilkin, A.; Straumal, B. B.; Protasova, S. G.; Gorji, S.; Straumal, A. B.; Katter, M.; Schütz, G.; Barezky, B. Grain Boundary Oxide Layers in NdFeB-Based Permanent Magnets. *Mater. Des.*, **2021**, *199*, 109417. https://doi.org/10.1016/j.matdes.2020.109417.
[31] Li, W. F.; Ohkubo, T.; Hono, K.; Sagawa, M. The Origin of Coercivity Decrease in Fine Grained Nd–Fe–B Sintered Magnets. *J. Magn. Magn. Mater.*, **2009**, *321* (8), 1100–1105. https://doi.org/10.1016/j.jmmm.2008.10.032.
[32] Marzun, G.; Bönnemann, H.; Lehmann, C.; Spliethoff, B.; Weidenthaler, C.; Barcikowski, S. Role of Dissolved and Molecular Oxygen on Cu and PtCu Alloy Particle Structure during Laser Ablation Synthesis in Liquids. *ChemPhysChem*, **2017**, *18* (9), 1175–1184. https://doi.org/10.1002/cphc.201601315.
[33] Kalus, M.-R.; Lanyumba, R.; Barcikowski, S.; Gökce, B. Discrimination of Ablation, Shielding, and Interface Layer Effects on the Steady-State Formation of Persistent Bubbles under Liquid Flow Conditions during Laser Synthesis of Colloids. *J. Flow Chem.*, **2021**, *11* (4), 773–792. https://doi.org/10.1007/s41981-021-00144-7.
[34] Schäfer, L.; Skokov, K.; Liu, J.; Maccari, F.; Braun, T.; Riegg, S.; Radulov, I.; Gassmann, J.; Merschroth, H.; Harbig, J.; et al. Design and Qualification of Pr–Fe–Cu–B Alloys for the Additive Manufacturing of Permanent Magnets. *Adv. Funct. Mater.*, **2021**, *31* (33), 2102148. https://doi.org/10.1002/adfm.202102148.
[35] Magnequench Inc. Material Data Sheet of MQP-S, 2006.
[36] Kozieł, T.; Pajor, K.; Gondek, Ł. Cooling Rate Evaluation during Solidification in the Suction Casting Process. *J. Mater. Res. Technol.*, **2020**, *9* (6), 13502–13508. https://doi.org/10.1016/j.jmrt.2020.09.082.
[37] Hooper, P. A. Melt Pool Temperature and Cooling Rates in Laser Powder Bed Fusion. *Addit. Manuf.*, **2018**, *22*, 548–559. https://doi.org/10.1016/j.addma.2018.05.032.
[38] Zhang, D.; Zhang, C.; Liu, J.; Chen, Q.; Zhu, X.; Liang, C. Carbon-Encapsulated Metal/Metal Carbide/Metal Oxide Core–Shell Nanostructures Generated by Laser Ablation of Metals in Organic Solvents. *ACS Appl. Nano Mater.*, **2019**, *2* (1), 28–39. https://doi.org/10.1021/acsanm.8b01541.
[39] Kawasaki, M. Laser-Induced Fragmentative Decomposition of Fine CuO Powder in Acetone as Highly Productive Pathway to Cu and Cu2O Nanoparticles. *J. Phys. Chem. C*, **2011**, *115* (12), 5165–5173. https://doi.org/10.1021/jp1095147.
[40] Fromme, T.; Tintrop, L. K.; Reichenberger, S.; Schmidt, T. C.; Barcikowski, S. Impact of Chemical and Physical Properties of Organic Solvents on the Gas and Hydrogen Formation during Laser Synthesis of Gold Nanoparticles. *ChemPhysChem*, *n/a* (n/a), e202300089. https://doi.org/10.1002/cphc.202300089.
[41] Nath, A.; Khare, A. Size Induced Structural Modifications in Copper Oxide Nanoparticles Synthesized via Laser Ablation in Liquids. *J. Appl. Phys.*, **2011**, *110* (4), 043111. https://doi.org/10.1063/1.3626463.
[42] Gondal, M. A.; Qahtan, T. F.; Dastageer, M. A.; Saleh, T. A.; Maganda, Y. W.; Anjum, D. H. Effects of Oxidizing Medium on the Composition, Morphology and Optical Properties of Copper Oxide Nanoparticles Produced by Pulsed Laser Ablation. *Appl. Surf. Sci.*, **2013**, *286*, 149–155. https://doi.org/10.1016/j.apsusc.2013.09.038.
[43] Neuenschwander, B.; Jaeggi, B.; Schmid, M.; Hennig, G. Surface Structuring with Ultra-Short Laser Pulses: Basics, Limitations and Needs for High Throughput. *Phys. Procedia*, **2014**, *56*, 1047–1058. https://doi.org/10.1016/j.phpro.2014.08.017.
[44] Wagener, P.; Schwenke, A.; Chichkov, B. N.; Barcikowski, S. Pulsed Laser Ablation of Zinc in Tetrahydrofuran: Bypassing the Cavitation Bubble. *J. Phys. Chem. C*, **2010**, *114* (17), 7618–7625. https://doi.org/10.1021/jp911243a.
[45] Nolte, S.; Kamlage, G.; Korte, F.; Bauer, T.; Wagner, T.; Ostendorf, A.; Fallnich, C.; Welling, H. Microstructuring with Femtosecond Lasers. *Adv. Eng. Mater.*, **2000**, *2* (1–2), 23–27. https://doi.org/10.1002/(SICI)1527-2648(200002)2:1/2<23::AID-ADEM23>3.0.CO;2-L.
[46] Thorstensen, J.; Erik Foss, S. Temperature Dependent Ablation Threshold in Silicon Using Ultrashort Laser Pulses. *J. Appl. Phys.*, **2012**, *112* (10), 103514. https://doi.org/10.1063/1.4766380.
[47] Vogel, A.; Linz, N.; Freidank, S.; Paltauf, G. Femtosecond-Laser-Induced Nanocavitation in Water: Implications for Optical Breakdown Threshold and Cell Surgery. *Phys. Rev. Lett.*, **2008**, *100* (3), 038102. https://doi.org/10.1103/PhysRevLett.100.038102.

[48] Wilms, M. B.; Streubel, R.; Frömel, F.; Weisheit, A.; Tenkamp, J.; Walther, F.; Barcikowski, S.; Schleifenbaum, J. H.; Gökce, B. Laser Additive Manufacturing of Oxide Dispersion Strengthened Steels Using Laser-Generated Nanoparticle-Metal Composite Powders. *Procedia CIRP*, **2018**, *74*, 196–200. https://doi.org/10.1016/j.procir.2018.08.093.

[49] Sepehri-Amin, H.; Ohkubo, T.; Nishiuchi, T.; Hirosawa, S.; Hono, K. Coercivity Enhancement of Hydrogenation–Disproportionation–Desorption–Recombination Processed Nd–Fe–B Powders by the Diffusion of Nd–Cu Eutectic Alloys. *Scr. Mater.*, **2010**, *63* (11), 1124–1127. https://doi.org/10.1016/j.scriptamat.2010.08.021.

[50] Gutfleisch, O. Controlling the Properties of High Energy Density Permanent Magnetic Materials by Different Processing Routes. *J. Phys. Appl. Phys.*, **2000**, *33* (17), R157. https://doi.org/10.1088/0022-3727/33/17/201.

[51] Woodcock, T. G.; Zhang, Y.; Hrkac, G.; Ciuta, G.; Dempsey, N. M.; Schrefl, T.; Gutfleisch, O.; Givord, D. Understanding the Microstructure and Coercivity of High Performance NdFeB-Based Magnets. *Scr. Mater.*, **2012**, *67* (6), 536–541. https://doi.org/10.1016/j.scriptamat.2012.05.038.

[52] Sepehri-Amin, H.; Une, Y.; Ohkubo, T.; Hono, K.; Sagawa, M. Microstructure of Fine-Grained Nd–Fe–B Sintered Magnets with High Coercivity. *Scr. Mater.*, **2011**, *65* (5), 396–399. https://doi.org/10.1016/j.scriptamat.2011.05.006.

[53] Knoch, K. G.; Le Calvez, A.; Qi, Q.; Leithe-Jasper, A.; Coey, J. M. D. Structure and Magnetic Properties of Nd6Fe13Cu. *J. Appl. Phys.*, **1993**, *73* (10), 5878–5880. https://doi.org/10.1063/1.353508.

[54] Tosoni, O.; Borges, E.; Reijonen, J.; Antikainen, A.; Schaefer, L.; Riegg, S.; Gutfleisch, O. High-Coercivity Copper-Rich Nd-Fe-B Magnets by Powder Bed Fusion Using Laser Beam Method. *Available SSRN Httpsssrncomabstract4149170*. https://doi.org/10.2139/ssrn.4149170.

[55] Camp, F. E.; Kim, A. S. Effect of Microstructure on the Corrosion Behavior of NdFeB and NdFeCoAlB Magnets. *J. Appl. Phys.*, **1991**, *70* (10), 6348–6350. https://doi.org/10.1063/1.349938.

[56] Sasaki, T. T.; Ohkubo, T.; Une, Y.; Kubo, H.; Sagawa, M.; Hono, K. Effect of Carbon on the Coercivity and Microstructure in Fine-Grained Nd–Fe–B Sintered Magnet. *Acta Mater.*, **2015**, *84*, 506–514. https://doi.org/10.1016/j.actamat.2014.10.047.

[57] Vial, F.; Joly, F.; Nevalainen, E.; Sagawa, M.; Hiraga, K.; Park, K. T. Improvement of Coercivity of Sintered NdFeB Permanent Magnets by Heat Treatment. *J. Magn. Magn. Mater.*, **2002**, *242–245*, 1329–1334. https://doi.org/10.1016/S0304-8853(01)00967-2.

[58] Jung, H. J.; Choi, M. Y. One-Pot Synthesis of Graphitic and Nitrogen-Doped Graphitic Layers on Nickel Nanoparticles Produced by Pulsed Laser Ablation in Liquid: Solvent as the Carbon and Nitrogen Source. *Appl. Surf. Sci.*, **2018**, *457*, 1050–1056. https://doi.org/10.1016/j.apsusc.2018.07.036.

[59] Reichenberger, S.; Marzun, G.; Muhler, M.; Barcikowski, S. Perspective of Surfactant-Free Colloidal Nanoparticles in Heterogeneous Catalysis. *ChemCatChem*, **2019**, *11* (18), 4489–4518. https://doi.org/10.1002/cctc.201900666.

Supporting information

To the manuscript of Gabriel et al. “Upscaled laser synthesis of copper nanoparticles in acetone to correlate the surface modification of Nd-Fe-B feedstock properties with part properties after full melting and rapid solidification”

Section 1: Laser setup and parameter study

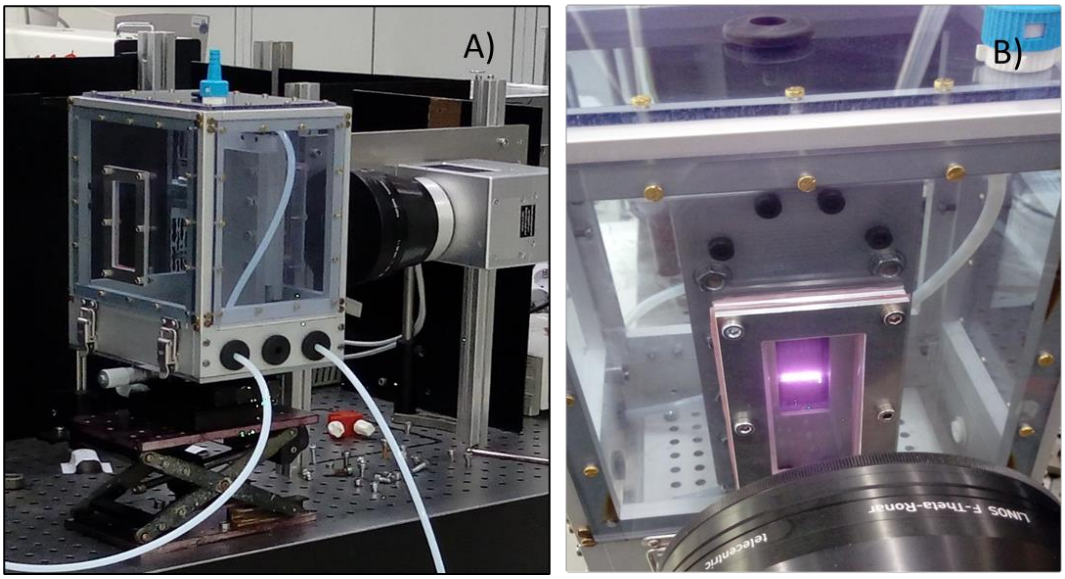

Figure S 1 Photographs of the production setup of laser ablation in liquids (LAL). A) production setup showing the Nitrogen-flooded safety chamber (210 x 260 x 180 mm) around the flow chamber, B) production setup showing the ablation process via pulsed laser beam scanning.

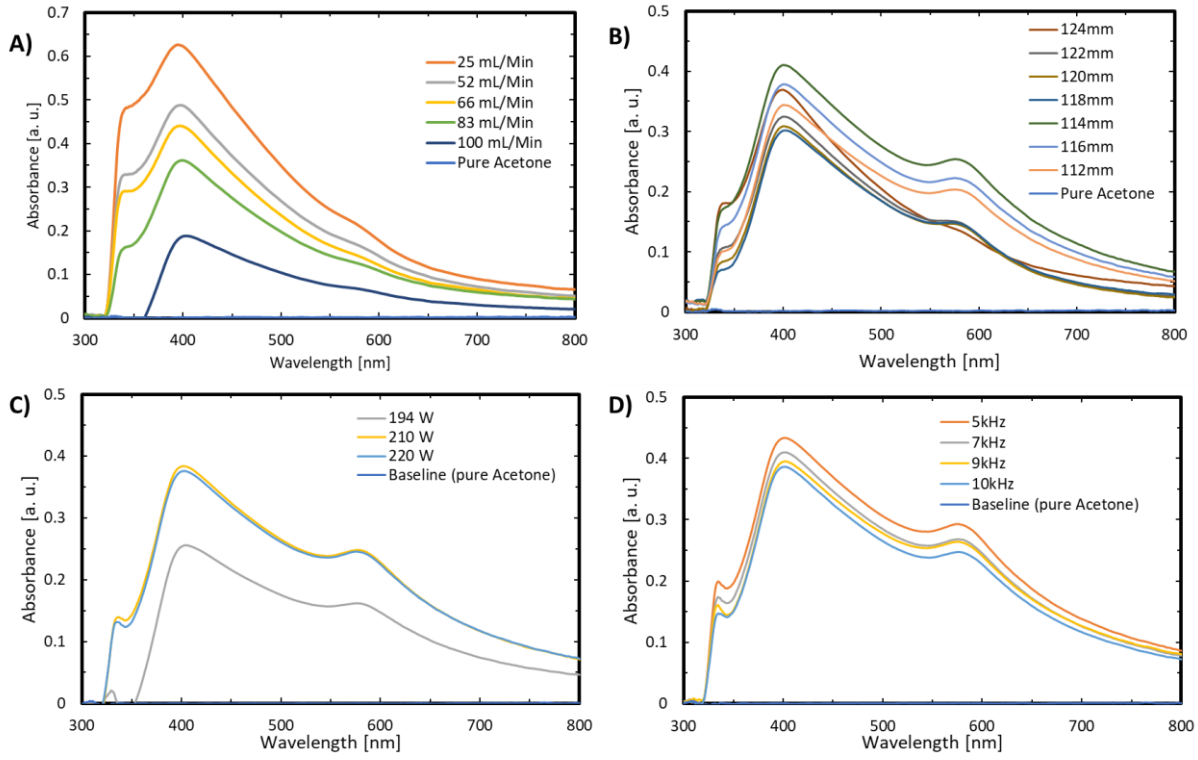

Figure S 2 UV-Vis extinction spectra of the process parameter study for LAL of Cu in acetone with the investigated values of A) volume flow, B) working distance (corresponding to spot size), C) laser power, and D) repetition rate.

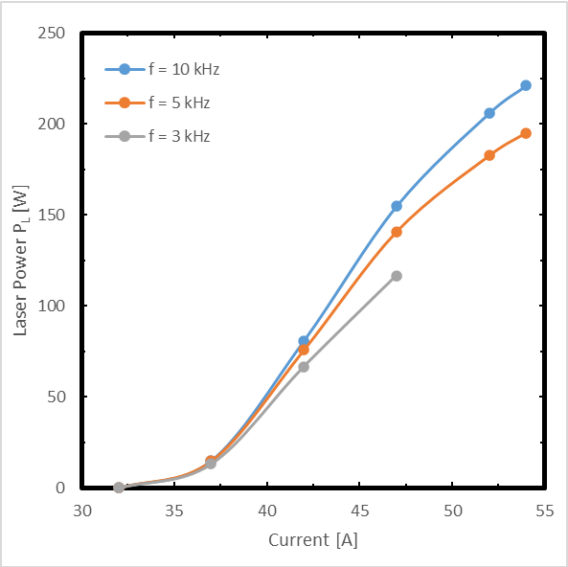

Figure S 3 Dependence of the achievable laser power PL by variation of the current and the repetition rate.

Section 2: Powder feedstock analysis

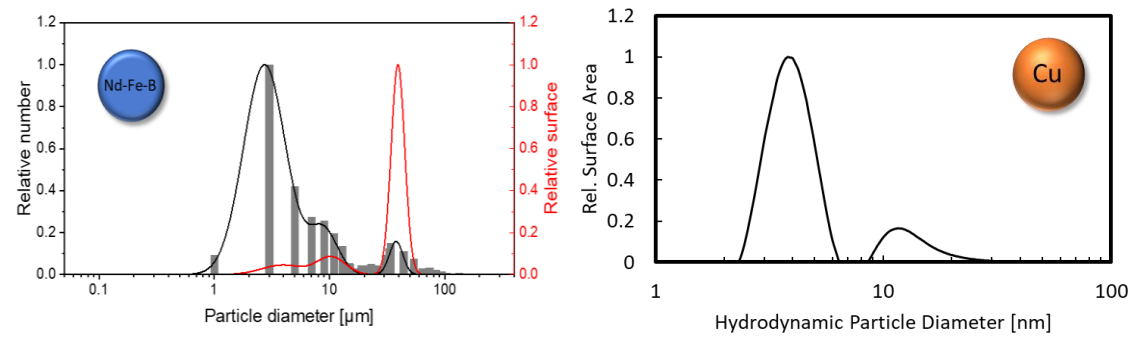

Figure S 4 Particles Size Distribution (PSD) analysis of pure MQP-S powder (via SEM image analysis) and Cu NPs (via ADC) ablated in acetone before mixing.

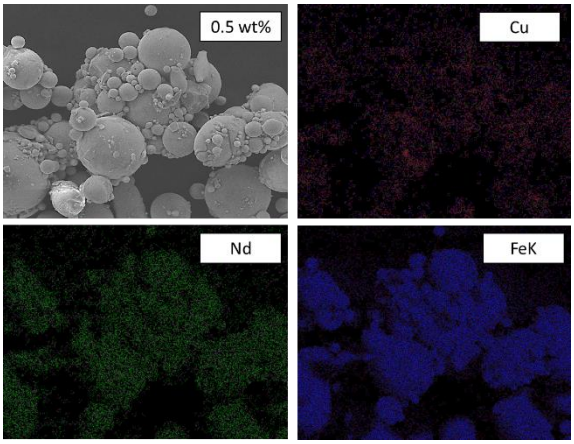

Figure S 5 EDX mapping of MQP-S MPs, decorated with 0.5 wt.% Cu NPs, A) SEM image of the exemplary area for the mapping of the elements, B) showing an even distribution of Cu on the surface, C) and D) showing the distribution of Nd and Fe of the Nd-Fe-B powder.

Table S 1 XRF analysis of Cu loadings after Cu NP additivation on MQP-S powder

Elements (wt.%)	Cu NPs loadings on MQP-S MPs			
	0.1	**0.5**	**1.0**	**2.5**
Fe	74.5	73.7	73.87	73.2
Nd	18.1	18.9	18.1	16.4
Co	3.0	2.7	2.49	1.9
Ti	1.9	2.1	1.95	1.9
Pr	2.0	2.0	1.97	1.8
Cu	0.3	0.5	1.4	4.6

Section 3: Magnetic performance

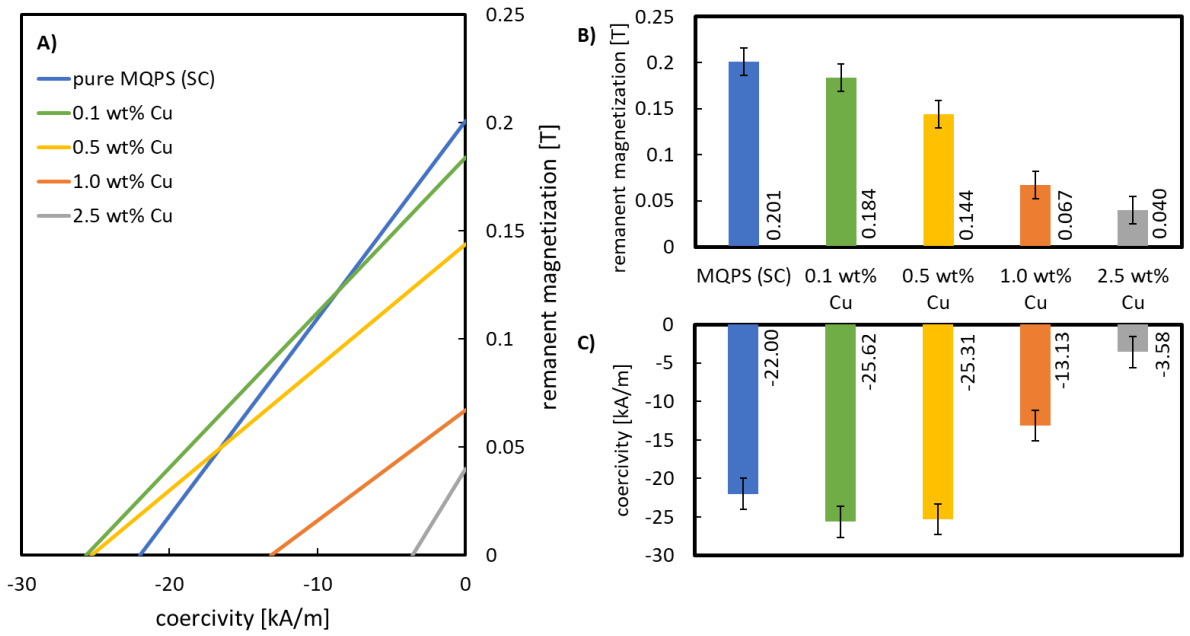

Figure S 6 A) Second quadrant of hysteresis curves of pure MQP-S with and without the addition of the loading series of Cu NPs after suction casting at room temperature. B) and C) comparison of the resulting magnetic properties depending on the addition of Cu NPs.